# Novel plasma-assisted low-temperature-processed SnO2 thin films for efficient flexible perovskite photovoltaics

Subbiah, Anand S.; Mathews, Nripan; Mhaisalkar, Subodh; Sarkar, Shaibal K.

2018

Subbiah, A. S., Mathews, N., Mhaisalkar, S., & Sarkar, S. K. (2018). Novel plasma-assisted low-temperature-processed SnO2 thin films for efficient flexible perovskite photovoltaics. ACS Energy Letters, 3(7), 1482-1491. doi:10.1021/acsenergylett.8b00692

https://hdl.handle.net/10356/142118

https://doi.org/10.1021/acsenergylett.8b00692

# Novel Plasma-Assisted Low-Temperature-Processed $SnO_2$ Thin Films for Efficient Flexible Perovskite Photovoltaics

Anand S. Subbiah,[a] Nripan Mathews,[b,c] Subodh Mhaisalkar,[b,c] Shaibal K. Sarkar*,[a]

[a]Department of Energy Science and Engineering, Indian Institute of Technology Bombay, Mumbai 400076, India.
[b]Energy Research Institute @ NTU (ERI@N), Research Techno Plaza, X-Frontier Block, Level 5, 50 Nanyang Drive, Singapore 637553.
[c]School of Materials Science and Engineering, Nanyang Technological University, Nanyang Avenue, Singapore 639798.

**Abstract**

The recent evolution of solution-processed hybrid organic–inorganic perovskite-based photovoltaic devices opens up the commercial avenue for high-throughput roll-to-roll manufacturing technology. To circumvent the thermal limitations that hinder the use of metal oxide charge transport layers on plastic flexible substrates in such technologies, we employed a relatively low-power nitrogen plasma treatment to achieve compact $SnO_2$ thin-film electrodes at near room temperature. The perovskite photovoltaic devices thus fabricated using $N_2$ plasma-treated $SnO_2$ performed on par with thermally annealed $SnO_2$ electrodes and resulted in a power conversion efficiency (PCE) of ca. 20.3% with stabilized power output (SPO) of ca. 19.1% on rigid substrates. Furthermore, the process is extended to realize flexible perovskite solar cells on indium tin oxide (ITO)-coated polyethylene terephthalate (PET) substrates with champion PCE of 18.1% (SPO ca. 17.1%), which retained ca. 90% of its initial performance after 1000 bending cycles. Our investigations reveal that deep ultraviolet irradiation associated with $N_2$ and $N_2O$ plasma emission plays a major role in obtaining good quality metal oxide thin films at lower temperatures and offers promise toward facile integration of a wide variety of metal oxides on flexible substrates.

The past decade has witnessed significant advances in the technological development of organic–inorganic lead halide perovskite solar cells (PSCs), which make possible the commercialization of solution-processed photovoltaic devices.(1,2) Conjunctional research efforts in material development,(3−6) process methodology,(7−9) and device configuration(10−13) have resulted in immense transformations in power conversion efficiency (PCE) from 3.8% in 2009(14) to 22.1% in 2017.(15) Such advancements have given way to long-desired flexible solar cells that retain extensive advantages in comparison to rigid substrates.(16−18) However, the major bottleneck in the realization of cost-effective flexible PSCs lies in establishing an alternative strategy to overcome the conventionally used thermal intensive process for oxide layer deposition.(19−23) Thermally stable flexible substrates such as titanium foil,(24,25) stainless steel fiber,(26) and flexible willow glass(27) are often used to overcome these process limitations with notable success; however, they are unlikely to render an economical solution and are currently limited by their availability.

From a commercial perspective, cheaper polymer plastic substrates such as polyethylene terephthalate (PET) and polyethylene naphthalate (PEN) are best suited for flexible perovskite devices.(16,28,29) Owing to their thermal limitations, developing the entire perovskite device architecture via reduced thermal intensive processes (<100 °C) has been a major challenge. Organic materials such as poly(3,4-ethylene dioxythiophene) polystyrenesulfonate (PEDOT:PSS);(30,31) phenyl-C61-butyric acid methyl ester (PCBM);(32,33) and at times

materials like C60,(34,35) graphene,(36) etc. are used as an alternative charge extraction layer with reduced process temperatures. Considering the limitations of most organic charge transport materials in terms of material cost and long-term stability,(37,38) an approach to produce quality metal oxide thin-film semiconductors at low temperatures would certainly benefit scalable techniques like roll-to-roll printing.

To achieve low-temperature deposition of metal oxides for their use as a charge extraction layer in PSCs, quite a few fabrication methodologies are being explored.(39−42) Recently, Kim et al. demonstrated a novel approach to develop metal oxide thin films by exposing the spin-coated metal precursor (metal salts dissolved in alcohol) films to deep ultraviolet (DUV) irradiation, which effectively circumvents the conventional annealing step.(43) Exposure to a high-power UV light (ca. 500 W) coupled with unintentional substrate heating facilitates the formation of a metal–oxide–metal (M–O–M) network followed by film densification. This relatively low-temperature methodology leads to good quality metal oxide thin films, which are suitable for many flexible applications.(43,44) This approach was lately adopted by Huang et al. to fabricate PSCs that employ DUV-treated tin oxide ($SnO_2$) as an electron transport layer (ETL) with methylammonium lead trihalide ($MAPbI_{3-x}Cl_x$) as an absorber, resulting in a device efficiency of 16.2%.(45) On a similar note, Zhu et al. utilized a rapid millisecond-pulsed photonically annealed $SnO_2$ layer, leading to 15% efficient PSCs.(46) Both techniques have realized the formation of $SnO_2$ ETL at relatively low substrate temperatures where the localized rise in material temperature supposedly does not affect the substrates. However, the device parameters obtained in these studies are comparatively lower than the one achieved using thermally annealed $SnO_2$ (TA-$SnO_2$) ETL, developed earlier.(47) Nevertheless, the possibility of achieving flexible polymer perovskite solar cells by making use of metal oxide thin films at reduced temperatures is yet to be demonstrated, though probably achievable.

Suitable energy band alignment, better optical transparency, higher charge carrier mobility, and easier processability with lower thermal budget favors $SnO_2$ as a better choice over the conventional titanium dioxide ($TiO_2$) as ETL in PSCs.(11,48,49) In the present study, we developed an alternate strategy for producing $SnO_2$ metal oxide semiconductors at near room temperature that involves low-power inductively coupled radio frequency (RF) plasma. In this method, sol–gel-coated $SnO_2$ thin films are activated using nitrogen plasma to break the alkoxy and hydroxy groups, which enables the formation of a metal–oxide–metal network. The $N_2$ plasma-treated $SnO_2$ (NPT-$SnO_2$) retains material properties comparable to those of TA-$SnO_2$. Furthermore, the modified NPT-$SnO_2$ ETL-based devices showed a significant improvement over TA-$SnO_2$ ETL-based devices on conventional FTO-coated rigid glass substrates with triple cation perovskite ($(FA_{0.83}MA_{0.17})_{0.95}Cs_{0.05}PbI_{2.5}Br_{0.5}$) as an absorber layer. The advantage offered by the NPT-$SnO_2$ compact layer in terms of the low processing temperatures was further explored by employing an indium tin oxide (ITO)-coated PET substrate, which resulted in highly efficient flexible devices with a champion PCE of 18.1% under 1 sun illumination.

Scheme 1 represents the formation of a tin oxide ($SnO_2$) thin film on top of FTO-coated glass substrates using the $N_2$ plasma treatment method employed in this study. Here, a solution containing 0.05 M tin(IV) chloride pentahydrate ($SnCl_4 \cdot 5H_2O$) in isopropyl alcohol (IPA) is spin-coated and subsequently exposed to 18 W $N_2$ RF-plasma under low vacuum (ca. 1 Torr) with varied exposure time. A detailed description of the process methodology is elaborated in the

Experimental Section in the Supporting Information. As a control experiment, similar spin-coated films are thermally annealed at ca. 180 °C for 60 min to form $SnO_2$ by thermal oxidation as reported earlier.(47) Both the $N_2$ plasma-treated (NPT-$SnO_2$) and thermally oxidized (TA-$SnO_2$) films are crystalline in nature, while the as-deposited films (AD-$SnO_2$) (spin-coated only) are amorphous, as indicated by the X-ray diffraction pattern (Figure SI-1a). Additionally, the spin-coated films are also exposed to $O_2$ plasma (OPT-$SnO_2$) while keeping the rest of the parameters unchanged to understand the effects of different plasma species and associated condensation mechanism, if there are any.

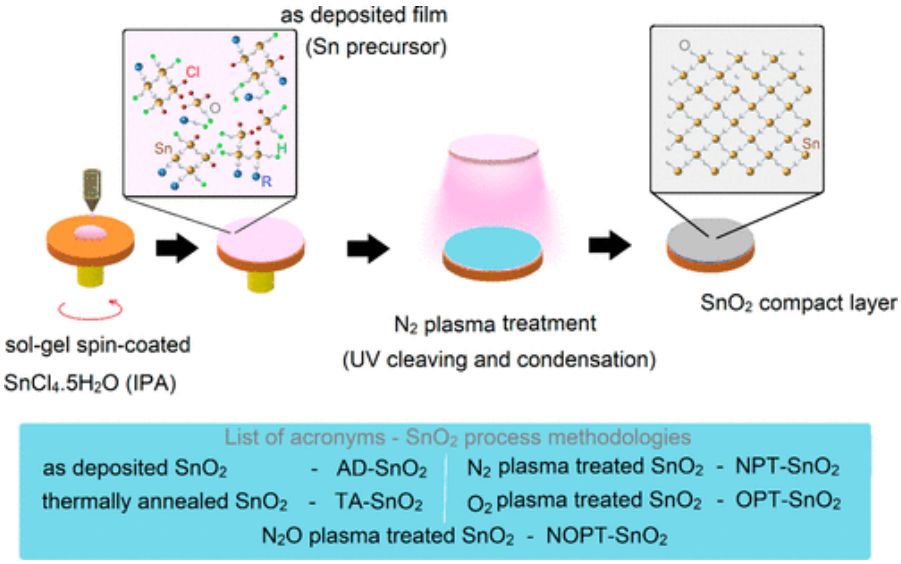


**Scheme 1.** Schematic Representation of the $SnO_2$ Thin-Film Fabrication Methodology Using a Modified Sol–Gel Technique by Employing Low-Power RF $N_2$ Plasma Exposure for 60 min in an Approximate Pressure of 1 Torr[a]

[a]The list of acronyms depicting the process methodologies used in this study for processing $SnO_2$ thin films is also provided.

X-ray photoemission spectroscopy (XPS) studies are carried out to understand the difference in chemical composition of the NPT-$SnO_2$ (18 W, 60 min) thin film in comparison to the AD-$SnO_2$, TA-$SnO_2$ (180 °C, 60 min) and OPT-$SnO_2$ (18 W, 60 min) thin films. The wide-range XPS survey spectra for all four samples are shown in Figure SI-3. Both NPT-$SnO_2$ and TA-$SnO_2$ films exhibited Sn 3d peaks corresponding to the $Sn^{4+}$ state with $3d_{3/2}$ at ca. 495.1 eV and $3d_{5/2}$ at ca. 486.7 eV, which are in agreement with previously reported values(45) (Figure SI-4 and Table SI-1). In contrast, the Sn 3d peaks of AD-$SnO_2$ and OPT-$SnO_2$ films shifted toward the higher binding energy (BE), indicating the possibility of Sn bonding with Cl, as chlorine is more electronegative than oxygen.

To estimate the relative presence and the chemical nature of the residual Cl that indicates conversion of the $SnCl_4$ metal precursor to $SnO_2$, a high energy resolution survey of Cl element is carried out on all four samples (Figure 1a). The Cl 2p peaks of NPT-$SnO_2$ and TA-$SnO_2$ films ($2p_{1/2}$ at ca. 200 eV and $2p_{3/2}$ at ca. 198.5 eV) are significantly reduced, indicating the minimal presence of the metal chloride precursor and hence better conversion to metal oxide in these films. Conversely, the AD-$SnO_2$ and OPT-$SnO_2$ samples show slightly shifted predominant Cl 2p peaks

($2p_{1/2}$ at ca. 200.5 eV and $2p_{3/2}$ at ca. 199 eV), implying the substantial presence of tin chloride precursor in their composition. Interestingly, the OPT-$SnO_2$ sample also showed a relatively small peak at ca. 206 eV, indicating the presence of chlorate $(ClO_3)^-$ ions in small quantities.(50) The formation of the chlorate ions is probably due to the interaction of reactive oxygen species from $O_2$ plasma treatment.

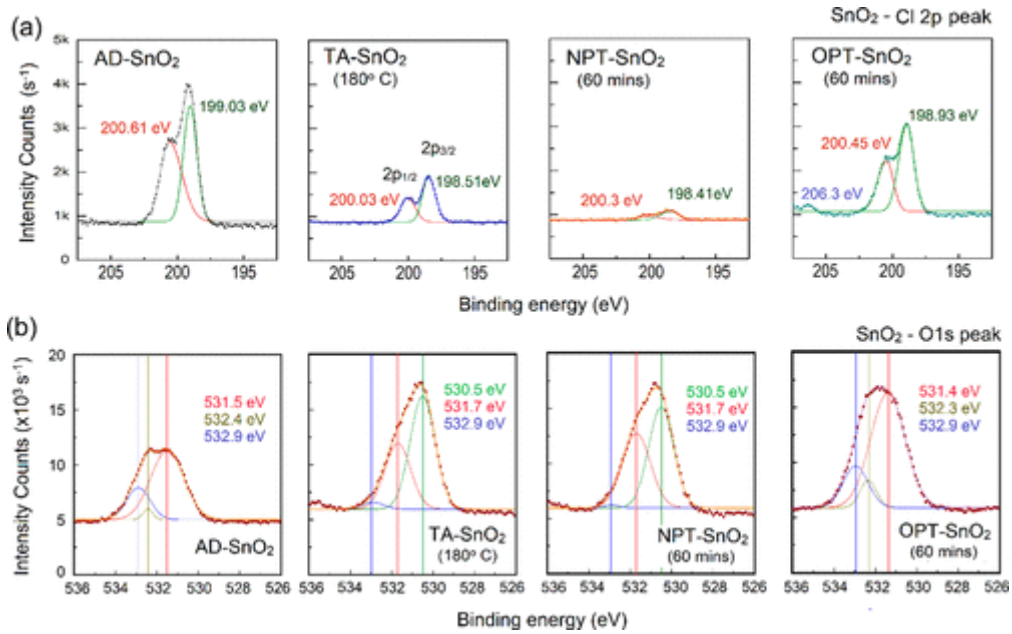


**Figure 1.** X-ray photoemission spectroscopy spectra (XPS) showing (a) chlorine Cl 2p peaks ($2p_{1/2}$ and $2p_{3/2}$) and (b) oxygen O 1s peak for all four variations of the $SnO_2$. Deconvolution of the O 1s peaks illustrated four different aspects of oxygen bonding at 530.5 eV (green line, oxygen atoms in M–O–M lattice), 531.5 eV (red line, oxygen bonding in M–O–C and oxygen atoms near vacancies), 532.4 eV (yellow line, carboxylate and chlorate ion bonds), and 532.9 eV (blue line, oxygen atoms in M–OH).

To understand the nature of the metal oxide states in all of the above four samples, the O 1s peaks in the high energy resolution survey are resolved into three major components, as depicted in Figure 1b. All four films showed a significant contribution of O 1s at around 531.5 ± 0.2 eV, which can be attributed to either the oxygen bonds in metal–oxy–carbonates (M–O–C) or oxygen atoms near oxygen vacancies ($M–O_{vac}$) (red line, Figure 1b).(43,45) However, the fractional contribution of this peak (red) reduced from ca. 73% in both AD-$SnO_2$ and OPT-$SnO_2$ films to around 36% and 45% in TA-$SnO_2$ and NPT-$SnO_2$ films, respectively (Table SI-2). In addition, the O 1s peak contribution corresponding to the M–O–M bonds at ca. 530.5 eV is observed only in TA-$SnO_2$ and NPT-$SnO_2$ films, with a major fractional contribution of 61% and 54%, respectively (green line, Figure 1b). In contrast, the same peak is nonexistent in both the AD-$SnO_2$ and OPT-$SnO_2$ samples, which essentially indicates the improper formation of the desired material. Also, the AD-$SnO_2$ and OPT-$SnO_2$ films showed a notable presence of metal hydroxide bonds (M–OH) at 532.9 eV (24% and 19%, respectively; blue line, Figure 1b), whereas a significant reduction of this peak is observed in the TA-$SnO_2$ and NPT-$SnO_2$ samples (ca. 3% and ca. 1%, respectively). Thus, the relative comparison of the O 1s peak suggests that TA-$SnO_2$ and NPT-$SnO_2$ films show similar chemical characteristics with larger M–O–M content alongside substantially reduced M–O–H and M–Cl bonds, indicating the better formation of the $SnO_2$ layer.

The conduction band (CB), valence band (VB), and Fermi level positions of the $SnO_2$ material thus formed for all four process methodologies are estimated using ultraviolet photoelectron spectroscopy (UPS) studies (Figures SI-5 and SI-6) while the band gap is determined by ultraviolet–visible (UV–vis) spectroscopy (Figure SI-2). Within the measurement error, the values provided in Figure SI-7 are near estimates to depict the energy band schematic of these materials. The relative position of the Fermi level indicates better carrier concentration and hence enhanced conductivity in the films formed by thermal annealing (TA-$SnO_2$) and the $N_2$ plasma route (NPT-$SnO_2$).

It is interesting that the $SnO_2$ film formation from Sn metal halide precursor materialized only in the presence of $N_2$ plasma, whereas the reactive species of $O_2$ plasma failed to aid in such transformation. Earlier studies have shown that in the presence of UV radiation, the formation mechanism involves the cleaving of partially formed metal alkoxy–hydroxyl bonds to form the M–O–M structure, followed by densification of the film.(43,44) In this case, we attribute the material formation to the energy offered by a significant DUV component (ca. 290–390 nm) in $N_2$ plasma emission alongside the NO* species emission (ca. 200–260 nm) under operating condition.(51) Similar to the mechanism described in previous studies,(43,44) here the plasma emission consisting of DUV photons imparts the necessary energy even at relatively low RF power to initiate the cleaving of metal alkoxy bonds. This phenomenon leads to M–O–M structure formation followed by subsequent removal of the carbon species by the plasma exposure resulting in film densification. For $O_2$ plasma, the emission spectrum at ca. 1 Torr operating pressure does not contain the necessary UV component to initiate the cleaving process,(52) because of which the film retains the original as-deposited composition to a larger extent. To support this hypothesis, the $N_2$ gas is replaced with $N_2O$, which offers UV emission similar to $N_2$ plasma. The $N_2O$ plasma-treated $SnO_2$ (NOPT-$SnO_2$) films performed on par with the NPT-$SnO_2$ in device configuration (discussed later in this Letter).

The formation of $SnO_2$ thin films at lower temperatures using $N_2$ plasma treatment enables their use as an electron transport layer in perovskite solar cells. The device architecture schematics and a scanning electron microscopy (SEM) cross-sectional image of the device is shown in Figure 2a. Figure 2b shows the as-measured (UPS and UV–vis studies) energy band diagram of the entire device [FTO-$SnO_2$-$((FA_{0.83}MA_{0.17})_{0.95}Cs_{0.05}PbI_{2.5}Br_{0.5})$-spiro-OMeTAD-Au]. The ability of cesium containing triple cation perovskite absorber with a tuned band gap of ca.1.7 eV to offer better stability and robustness alongside favorable band energy alignment with $SnO_2$ made it a preferred choice over commonly used $MAPbI_3$ perovskite absorber.(11) Details on the complete device fabrication procedure are provided in Experimental Section in the Supporting Information. On average, the NPT-$SnO_2$-based devices offered better open-circuit potential ($V_{OC}$; 1.1 ± 0.03 V) and fill factor (FF; 0.82 ± 0.022) over TA-$SnO_2$-based devices ($V_{OC}$, 1.07 ± 0.029 V; FF, 0.81 ± 0.014) (Table SI-3) under 1 sun illumination. A histogram of device efficiencies (BS conditions) revealing better device performance and narrower distribution of NPT-$SnO_2$-based devices over TA-$SnO_2$-based devices is shown in Figure 2c. The light current–voltage ($J$–$V$) characteristics of the champion devices on FTO-coated rigid glass substrates, obtained using a 500 $mV \cdot s^{-1}$ scan rate at 100 $mW \cdot cm^{-2}$ illumination is depicted in Figure 2d. The NPT-$SnO_2$-based devices exhibited a champion PCE of 20.3% with a $V_{OC}$ of ca. 1.12 V, FF of ca. 0.83, and a short-circuit current density ($J_{SC}$) of ca. 21.82 $mA \cdot cm^{-2}$ under BS conditions, whereas the TA-$SnO_2$-

based devices showed a champion PCE of 19.9% with a $V_{OC}$ of ca. 1.08 V, FF of ca. 0.81, and $J_{SC}$ of ca. 22.9 mA·cm$^{-2}$. The NPT-$SnO_2$ champion device had a stable power output (SPO) of 19.1% over a period of 200 s, which is considerably better than that of the TA-$SnO_2$ device with an SPO of 18.3% (Figure 2d, insets). The average increase in the PCE and $V_{OC}$ of the NPT-$SnO_2$ devices over the TA-$SnO_2$ devices points toward the possibility of a marginal difference in the quality of these materials and their interfaces. It is also important to mention that both devices exhibited a significantly stable power output under continuous maximum power point operation upon encapsulation. The NPT-$SnO_2$ device showed no degradation of the stable power output at 1 sun illumination over a period of 2 h under the ambient operating conditions as shown in Figure SI-9.

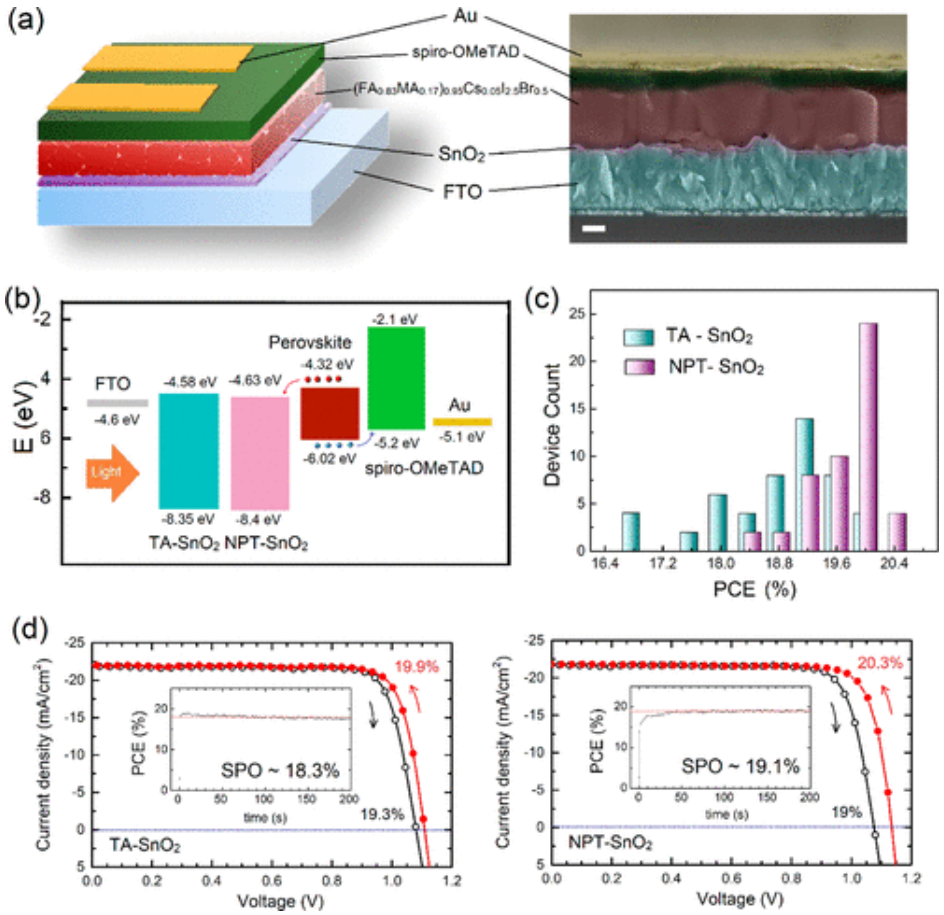


**Figure 2.** (a) Illustration of the planar perovskite solar cell employed in this report alongside SEM cross-sectional image of a planar device using NPT-$SnO_2$ as ETL (scale bar: 200 nm). (b) Proposed energy band schematic of the planar mixed cation perovskite absorber-based solar cell from UPS and band gap calculations (c) Device efficiency histogram obtained from backward scan (BS) under 1 sun illumination for different batches comprising a total of 50 devices to illustrate the difference in performance arising from TA-$SnO_2$ and NPT-$SnO_2$ ETL. (d) Light *J*–*V* characteristics of planar perovskite solar cells at 100 mW·cm$^{-2}$ (1 sun) intensity employing TA-$SnO_2$ and NPT-$SnO_2$ layers as ETL in both forward (FS) and backward scan (BS) directions delivering a PCE of 19.9% (BS) and 20.3% (BS), respectively. Inset: Stable power output (SPO) of both the devices under maximum power point during continuous illumination for 200 s.

The light *J*–*V* characteristics of both these devices at different illumination intensities are shown in Figure SI-10. The light ideality factors estimated from the intensity-dependent open-circuit potential for both devices exhibit a similar value, as shown in Figure 3b.(53) However, the NPT-$SnO_2$-based devices exhibited better robustness toward the scan rate variations in current–voltage characteristics, as shown in the Figure SI-11. Also, the transient $V_{OC}$ decay measurement reveals a relatively faster decay for the NPT-$SnO_2$ devices with an average decay lifetime of ($\tau_{decay}$) ca. 0.86 s, whereas the TA-$SnO_2$ devices exhibited a $\tau_{decay}$ of ca. 12.4 s (Figure 3a). The decay parameters obtained from biexponential decay fitting are provided in the inset. It is likely that the decrement in decay lifetime of NPT-$SnO_2$ devices is related to the reduced charge trapping, back recombination, and ion accumulation at the $SnO_2$–perovskite interface.(54,55)

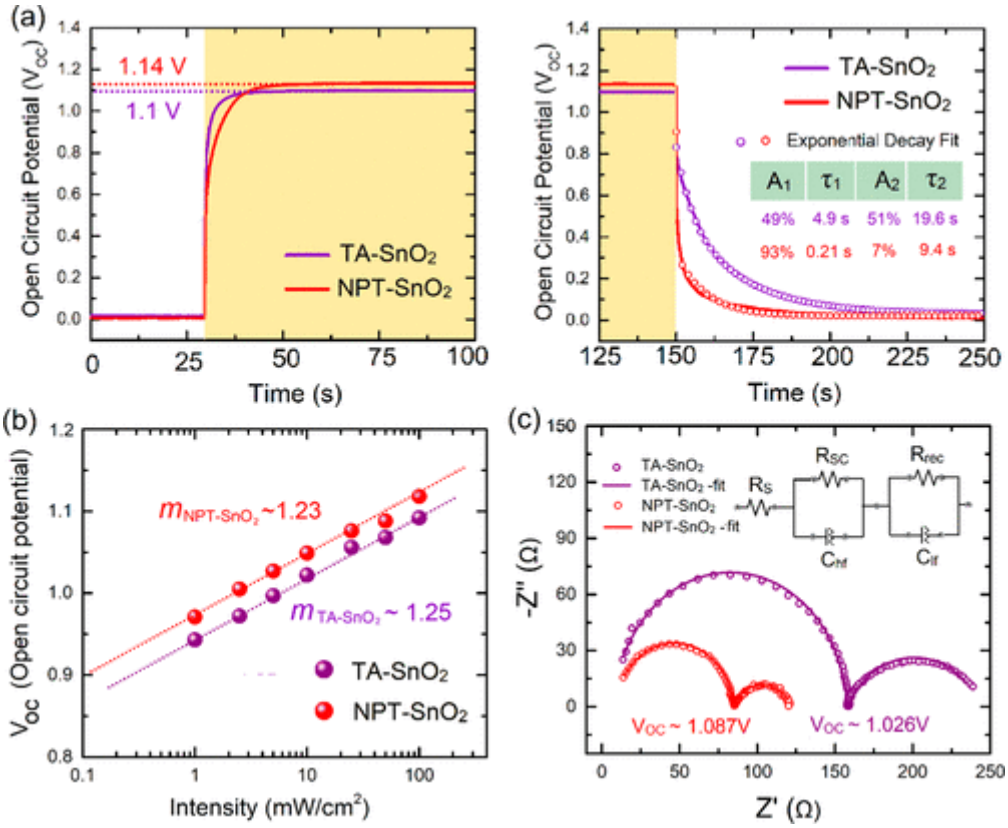


**Figure 3.** (a) Transient open-circuit potential ($V_{OC}$) measurement of both devices in seconds scale to establish the differences in rise and decay time periods of the $V_{OC}$ indicating variations in charge accumulation and detrapping at the $SnO_2$/perovskite interface. (b) Open-circuit potential of TA-$SnO_2$ and NPT-$SnO_2$ at different illumination intensities with a linear fit to extract the light ideality diode factor for both devices. (c) Nyquist plots from impedance spectroscopy (IS) under open-circuit potential at 1 sun illumination over a frequency range of 250 kHz to 1 mHz for both TA-$SnO_2$ and NPT-$SnO_2$-based devices. (Inset: Equivalent circuit diagram model used for fitting the impedance spectroscopy measurement).

To understand the relative differences in perovskite–$SnO_2$ interfaces, impedance spectroscopy (IS) measurement is performed for both NPT-$SnO_2$ and TA-$SnO_2$ devices over different applied potentials under 1 sun illumination. The IS spectra of both devices at $V_{OC}$ are depicted in Figure 3c alongside the model circuit adapted to understand the $SnO_2$–perovskite interface resistance, series

resistance, and recombination resistance (inset).(56,57) The IS spectra at open-circuit potential exhibits an arc of a smaller radius at the higher frequencies for the NPT-$SnO_2$ device in comparison to the TA-$SnO_2$ device, indicating a better $SnO_2$-perovskite interface for charge injection. Also, the $R_S$ (series resistance) extracted from fitting IS spectra at different bias potentials shows that the NPT-$SnO_2$ device experiences a series resistance (ca. 3 Ω) that is smaller than that of the TA-$SnO_2$ device (ca. 12 Ω) (Figure SI-12). The NPT-$SnO_2$-based device exhibits smaller values of selective contact resistance ($R_{SC}$) and recombination resistance ($R_{rec}$) at the recombination regime near the $V_{OC}$ operation point. However, as the conditions approach the charge transport regime under lower bias, the value of both $R_{SC}$ and $R_{rec}$ increases drastically in NPT-$SnO_2$ devices (Figure SI-12). With such variations in $R_{SC}$ and $R_{rec}$, the IS measurements certainly indicate that the NPT-$SnO_2$ device offers marginally better $SnO_2$–perovskite interface in comparison to the TA-$SnO_2$ device, resulting in slightly better photovoltaic device parameters.

A comparison of the photovoltaic performances of as-deposited, thermal, $N_2$ plasma, $O_2$ plasma, and $N_2O$ plasma-treated $SnO_2$ devices in planar rigid FTO-based architecture is shown in Figure 4a. Histogram of the various device parameters obtained using the different post-treatment methodologies are shown in Figure 4b, and the parameters are listed Table SI-3. Although all of the different postprocessing conditions for $SnO_2$ reveal a similar device morphology under SEM cross section (Figure SI-13), their photovoltaic performance greatly varies. The devices employing AD-$SnO_2$ and OPT-$SnO_2$ ETL demonstrated inferior device characteristics in comparison to the other methodologies. The effect of incomplete materialization of $SnO_2$ in AD-$SnO_2$- and OPT-$SnO_2$-based devices can be easily visualized by the shallow slopes ($R_S$) of their IV characteristics (Figure 4a). Also, their resistive nature is revealed by comparing their IS spectra at $V_{OC}$ under 1 sun illumination with that of NOPT-$SnO_2$ in Figure SI-14. Devices employing NOPT-$SnO_2$ exhibited a champion PCE of 19.95% (BS condition), which is comparable to that of NPT-$SnO_2$-based devices. These devices also retain a slightly better $V_{OC}$ distribution in comparison to the TA- $SnO_2$ devices, a similarity they share with NPT-$SnO_2$ devices. The success of the NOPT-$SnO_2$-based devices endorses our hypothesis that DUV emission from $N_2$ plasma is vital for the initial cleaving of metal alkoxy and metal hydroxyl bonds, resulting in compact $SnO_2$ thin films. Optimization of the plasma exposure time for NPT-$SnO_2$-based devices is shown in Figure SI-15, and the device parameters are listed in Table SI-4.

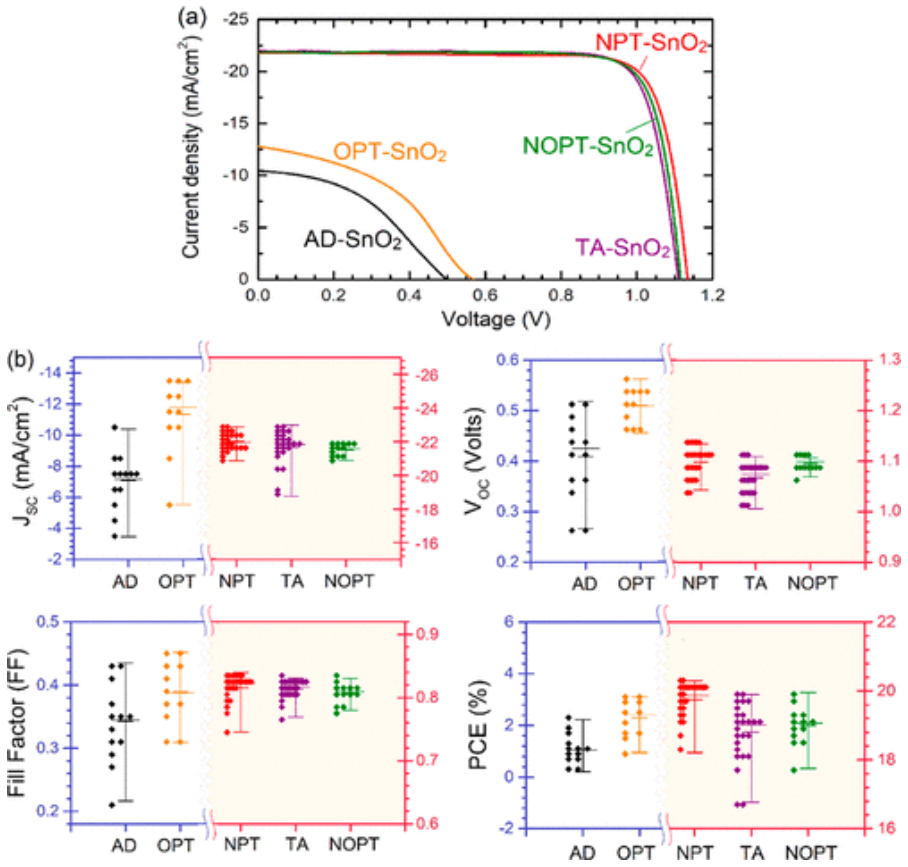


**Figure 4.** (a) Champion light *J*–*V* characteristics (BS) obtained by employing AD-$SnO_2$, TA-$SnO_2$, NPT-$SnO_2$, OPT-$SnO_2$, and NOPT-$SnO_2$ layers as ETLs in planar perovskite configuration. (b) Histograms of the device parameters $J_{SC}$, $V_{OC}$, FF, and PCE obtained from a batch of devices under various process conditions of the $SnO_2$ layer.

To exploit the advantages of low-temperature-processed NPT-$SnO_2$ as an ETL, we employed it on flexible ITO-PET substrates. Figure 5a shows the fabricated flexible PSCs with $[(FA_{0.83}MA_{0.17})_{0.95}Cs_{0.05}PbI_{2.5}Br_{0.5}]$ perovskite as absorber and spiro-OMeTAD as the HTL. After $SnO_2$ ETL deposition, an ultrathin layer of mesoporous alumina ($Al_2O_3$) is introduced by spin coating and subsequent exposure to low-power RF $N_2$ plasma (60 min) to effectively deal with issues like pinhole formation on the substrates. The SEM cross section of the device on flexible ITO substrates and the device schematic is shown in Figure 5b,c. The flexible devices offered a champion PCE of 18.1% under BS conditions, with a $V_{OC}$ of ca. 1.05 V, FF of ca. 0.76, $J_{SC}$ of ca. 22.8 mA·cm$^{-2}$, and SPO of ca. 17.1%, as shown in Figure 5d. To ensure the compatibility of the process for practical applications, the devices are subjected to a (manual) bending cycle test for 1000 cycles (see Figure 5a); the device performance parameters are listed in Figures 5e and SI-16. The device retained 90% of their initial PCE after 1000 cycles of bending, with the major loss in PCE arising from a drop in the FF (Table SI-6). Transient $V_{OC}$ decay measurement for the flexible devices (Figure 5f) exhibited a decay lifetime ($\tau_{decay}$) of ca. 0.8 s, similar to the value obtained for rigid FTO-based NPT-$SnO_2$ devices. Figure 5g shows the standard device parameter histogram obtained from a batch of 24 devices, illustrating the repeatability of the fabrication process. The devices showed an average $V_{OC}$ of 1.025 ± 0.011 V, which is better than most reported values regarding flexible substrates, with an overall average PCE of 16.8% ± 0.88% (Table SI-5).

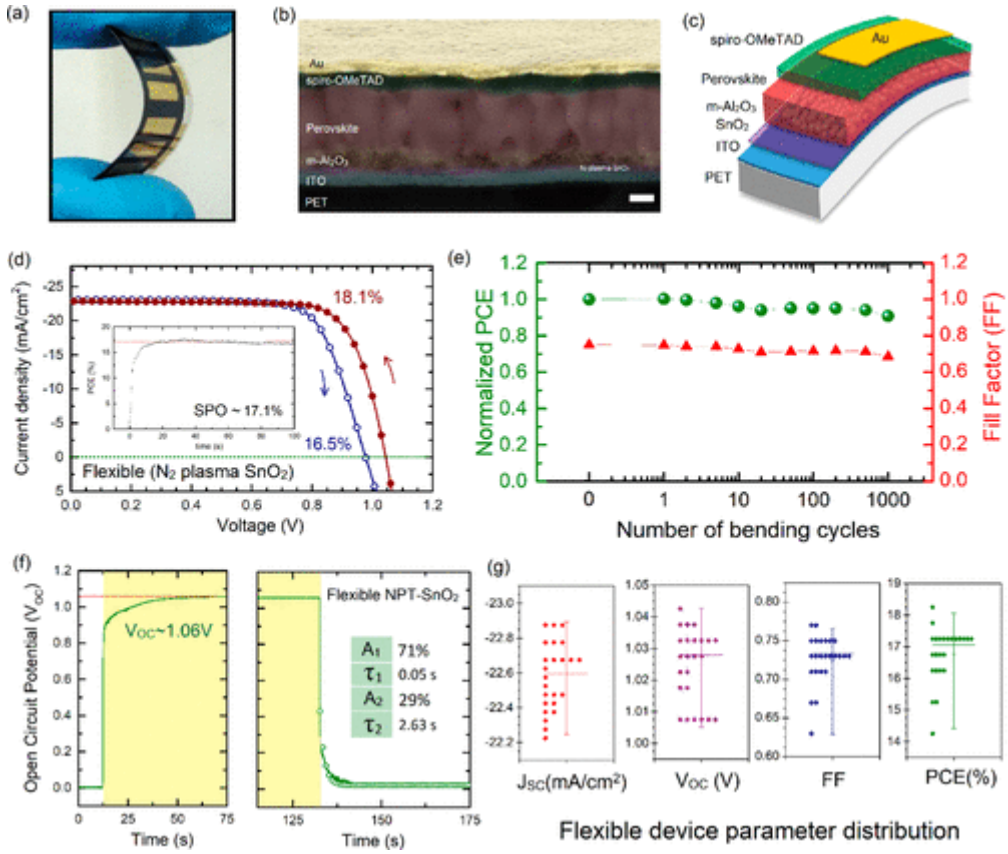


**Figure 5.** (a) Photograph depicting the flexible nature of the devices fabricated using room-temperature NPT-$SnO_2$ ETL. (b) SEM cross-sectional image of PET/ITO/NPT-$SnO_2$/m-$Al_2O_3$/$((FA_{0.83}MA_{0.17})_{0.95}Cs_{0.05}PbI_{2.5}Br_{0.5})$/spiro-OMeTAD/Au flexible device. (c) Device architecture schematic of the flexible device fabricated in this Letter. (d) Champion light *J*–*V* characteristics of the flexible device with PCE of 18.1% (BS) and a stable power output efficiency of 17.1% under 1 sun illumination. (e) Normalized device efficiency and fill factor of the flexible device being subjected to 1000 bending cycles (measured from BS). (f) Transient $V_{OC}$ measurements in seconds scale to illustrate the associated rise and decay constants. (g) Histogram of the various device parameters extracted from a batch of 24 flexible devices.

The IS measurements revealed an $R_S$ of ca. 27 Ω for flexible devices, which is significantly larger than the ones obtained for rigid FTO-based devices. This is primarily due to the fact that the sheet resistance of rigid FTO substrates is around 7 Ω/sq, whereas that of ITO-coated PET substrates is as high as 60 Ω/sq. The recombination resistance ($R_{rec}$) is also found to be on the lower side in the charge transport regime than with the FTO substrates, and it effectively contributed to the reduced FF observed for these devices. A list of all the parameters obtained at different bias potentials for the flexible devices is provided in Figure SI-17.

In conclusion, we demonstrated a modified methodology to fabricate metal oxide ($SnO_2$) charge transport layer via the sol–gel technique at room temperature with the help of low-power $N_2$ and $N_2O$ RF plasma post-treatment. The formation of a better quality $SnO_2$ compact layer using this method can be attributed to DUV emission signatures associated with the $N_2$ and $N_2O$ species. The high-energy UV photons facilitate the initial cleavage of metal alkoxy and hydroxyl groups,

leading to the formation of the M–O–M framework. Our modified technique yielded highly efficient PSCs with a PCE of 20.3% under BS conditions on rigid FTO substrates. The device and interface properties are superior to those of the conventionally used thermally annealed $SnO_2$ layers. Additionally, the ability to obtain room-temperature-processed $SnO_2$ compact layers has enabled us to use them on flexible ITO-PET substrates, resulting in highly efficient flexible devices with a PCE of 18.1% (BS). These flexible devices have shown excellent durability because they retained 90% of their initial PCE after 1000 bending cycles. The use of plasma-based post-treatment is a cost-effective route to fabricate various metal oxide charge transport layers at reduced temperatures, which can be used with flexible substrates. This will, in turn, facilitate the commercialization of perovskite devices using high-throughput roll-to-roll processing techniques in the future.

## Acknowledgement

This Letter is based upon work supported under the US-India Partnership to Advance Clean Energy-Research (PACE-R) for the Solar Energy Research Institute for India and the United States (SERIIUS), funded jointly by the U.S. Department of Energy (Office of Science, Office of Basic Energy Sciences, and Energy Efficiency and Renewable Energy, Solar Energy Technology Program, under Subcontract DE-AC36-08GO28308 to the National Renewable Energy Laboratory, Golden, Colorado) and the Government of India, through the Department of Science and Technology under Subcontract IUSSTF/JCERDC-SERIIUS/2012 dated 22nd November 2012. The authors acknowledge the funding from the Singapore National Research Foundation through the Singapore–Berkeley Research Initiative for Sustainable Energy (Sin-BeRISE) CREATE Program and the Competitive Research Program: NRF-CRP14-2014-03. This work is also partially funded by Ministry of New and Renewable Energy, Government of India. S.K.S. thanks Vikas Mathe for valuable discussions.

## References

(1) Service, R. F. Perovskite solar cells gear up to go commercial. Science 2016, 354 (6317), 1214−1215.

(2) Ono, L. K.; Park, N.-G.; Zhu, K.; Huang, W.; Qi, Y. Perovskite Solar Cells□Towards Commercialization. ACS Energy Lett. 2017, 2 (8), 1749−1751.

(3) Eperon, G. E.; Burlakov, V. M.; Docampo, P.; Goriely, A.; Snaith, H. J. Morphological Control for High Performance, SolutionProcessed Planar Heterojunction Perovskite Solar Cells. Adv. Funct. Mater. 2014, 24 (1), 151−157.

(4) Noh, J. H.; Im, S. H.; Heo, J. H.; Mandal, T. N.; Seok, S. I. Chemical Management for Colorful, Efficient, and Stable Inorganic− Organic Hybrid Nanostructured Solar Cells. Nano Lett. 2013, 13 (4), 1764−1769.

(5) Mitzi, D. B. Synthesis, Structure, and Properties of OrganicInorganic Perovskites and Related Materials. Prog. Inorg. Chem. 2007, 48, 1−121.

(6) Jesper Jacobsson, T.; Correa-Baena, J.-P.; Pazoki, M.; Saliba, M.; Schenk, K.; Gratzel, M.; Hagfeldt, A. Exploration of the Compositional Space for Mixed Lead Halogen Perovskites for High Efficiency Solar Cells. Energy Environ. Sci. 2016, 9 (5), 1706−1724.

(7) Paek, S.; Schouwink, P.; Athanasopoulou, E. N.; Cho, K. T.; Grancini, G.; Lee, Y.; Zhang, Y.; Stellacci, F.; Nazeeruddin, M. K.; Gao, P. From Nano- to Micrometer Scale: The Role of Antisolvent Treatment on High Performance Perovskite Solar Cells. Chem. Mater. 2017, 29 (8), 3490−3498.

(8) Chen, Q.; Zhou, H.; Hong, Z.; Luo, S.; Duan, H.-S.; Wang, H.- H.; Liu, Y.; Li, G.; Yang, Y. Planar Heterojunction Perovskite Solar Cells via Vapor-Assisted Solution Process. J. Am. Chem. Soc. 2014, 136 (2), 622−625.

(9) Zhou, Y.; Yang, M.; Wu, W.; Vasiliev, A. L.; Zhu, K.; Padture, N. P. Room-temperature Crystallization of Hybrid-Perovskite Thin Films via Solvent−Solvent Extraction for High-Performance Solar Cells. J. Mater. Chem. A 2015, 3 (15), 8178−8184.

(10) Saliba, M.; Matsui, T.; Seo, J.-Y.; Domanski, K.; Correa-Baena, J.-P.; Nazeeruddin, M. K.; Zakeeruddin, S. M.; Tress, W.; Abate, A.; Hagfeldt, A.; et al. Cesium-Containing Triple Cation Perovskite Solar Cells: Improved Stability, Reproducibility and High Efficiency. Energy Environ. Sci. 2016, 9 (6), 1989−1997.

(11) Correa Baena, J. P.; Steier, L.; Tress, W.; Saliba, M.; Neutzner, S.; Matsui, T.; Giordano, F.; Jacobsson, T. J.; Srimath Kandada, A. R.; Zakeeruddin, S. M.; et al. Highly Efficient Planar Perovskite Solar Cells through Band Alignment Engineering. Energy Environ. Sci. 2015, 8 (10), 2928−2934.

(12) Ito, S.; Tanaka, S.; Vahlman, H.; Nishino, H.; Manabe, K.; Lund, P. Carbon-Double-Bond-Free Printed Solar Cells from TiO2/ CH3NH3PbI3/CuSCN/Au: Structural Control and Photoaging Effects. ChemPhysChem 2014, 15 (6), 1194−1200.

(13) Zhang, F.; Yang, X.; Wang, H.; Cheng, M.; Zhao, J.; Sun, L. Structure Engineering of Hole-Conductor Free Perovskite-Based Solar Cells with Low-temperature-processed Commercial Carbon Paste as Cathode. ACS Appl. Mater. Interfaces 2014, 6 (18), 16140−16146.

(14) Kojima, A.; Teshima, K.; Shirai, Y.; Miyasaka, T. Organometal Halide Perovskites as Visible-Light Sensitizers for Photovoltaic Cells. J. Am. Chem. Soc. 2009, 131 (17), 6050−6051.

(15) Yang, W. S.; Park, B.-W.; Jung, E. H.; Jeon, N. J.; Kim, Y. C.; Lee, D. U.; Shin, S. S.; Seo, J.; Kim, E. K.; Noh, J. H.; et al. Iodide Management in Formamidinium-Lead-Halide−Based Perovskite Layers for Efficient Solar Cells. Science 2017, 356 (6345), 1376−1379.

(16) Di Giacomo, F.; Fakharuddin, A.; Jose, R.; Brown, T. M. Progress, Challenges and Perspectives in Flexible Perovskite Solar Cells. Energy Environ. Sci. 2016, 9 (10), 3007−3035.

(17) Liu, D.; Kelly, T. L. Perovskite Solar Cells with a Planar Heterojunction Structure Prepared using Room-Temperature Solution Processing Techniques. Nat. Photonics 2014, 8 (2), 133−138.

(18) Park, M.; Kim, J.-Y.; Son, H. J.; Lee, C.-H.; Jang, S. S.; Ko, M. J. Low-temperature Solution-Processed Li-Doped Sno2 as an Effective Electron Transporting Layer for High-Performance Flexible and Wearable Perovskite Solar Cells. Nano Energy 2016, 26, 208−215.

(19) Yang, G.; Tao, H.; Qin, P.; Ke, W.; Fang, G. Recent Progress in Electron Transport Layers for Efficient Perovskite Solar Cells. J. Mater. Chem. A 2016, 4 (11), 3970−3990.

(20) Mahmood, K.; Sarwar, S.; Mehran, M. T. Current Status of Electron Transport Layers in Perovskite Solar Cells: Materials and Properties. RSC Adv. 2017, 7 (28), 17044−17062.

(21) Liu, D.; Li, S.; Zhang, P.; Wang, Y.; Zhang, R.; Sarvari, H.; Wang, F.; Wu, J.; Wang, Z.; Chen, Z. D. Efficient Planar Heterojunction Perovskite Solar Cells with Li-Doped Compact TiO2 Layer. Nano Energy 2017, 31, 462−468.

(22) Yang, W. S.; Noh, J. H.; Jeon, N. J.; Kim, Y. C.; Ryu, S.; Seo, J.; Seok, S. I. High-Performance Photovoltaic Perovskite Layers Fabricated through Intramolecular Exchange. Science 2015, 348 (6240), 1234−1237.

(23) Qin, P.; Domanski, A. L.; Chandiran, A. K.; Berger, R.; Butt, H. J.; Dar, M. I.; Moehl, T.; Tetreault, N.; Gao, P.; Ahmad, S.; et al. Yttrium-substituted Nanocrystalline TiO2 Photoanodes for Perovskite based Heterojunction Solar Cells. Nanoscale 2014, 6 (3), 1508−1514.

(24) Xiao, Y.; Han, G.; Zhou, H.; Wu, J. An Efficient Titanium Foil based Perovskite Solar Cell: Using a Titanium Dioxide Nanowire Array Anode and Transparent Poly(3,4-Ethylenedioxythiophene) Electrode. RSC Adv. 2016, 6 (4), 2778−2784.

(25) Lee, M.; Jo, Y.; Kim, D. S.; Jeong, H. Y.; Jun, Y. Efficient, Durable and Flexible Perovskite Photovoltaic Devices with AgEmbedded ITO as the Top Electrode on a Metal Substrate. J. Mater. Chem. A 2015, 3 (28), 14592−14597.

(26) He, S.; Qiu, L.; Fang, X.; Guan, G.; Chen, P.; Zhang, Z.; Peng, H. Radically Grown Obelisk-like ZnO Arrays for Perovskite Solar Cell Fibers and Fabrics through a Mild Solution Process. J. Mater. Chem. A 2015, 3 (18), 9406−9410.

(27) Dou, B.; Miller, E. M.; Christians, J. A.; Sanehira, E. M.; Klein, T. R.; Barnes, F. S.; Shaheen, S. E.; Garner, S. M.; Ghosh, S.; Mallick, A.; et al. High-Performance Flexible Perovskite Solar Cells on Ultrathin Glass: Implications of the TCO. J. Phys. Chem. Lett. 2017, 8 (19), 4960−4966.

(28) Heo, J. H.; Lee, M. H.; Han, H. J.; Patil, B. R.; Yu, J. S.; Im, S. H. Highly Efficient Low Temperature Solution Processable Planar Type CH3NH3PbI3 Perovskite Flexible Solar Cells. J. Mater. Chem. A 2016, 4 (5), 1572−1578.

(29) Shin, S. S.; Yang, W. S.; Noh, J. H.; Suk, J. H.; Jeon, N. J.; Park, J. H.; Kim, J. S.; Seong, W. M.; Seok, S. I. High-Performance Flexible Perovskite Solar Cells Exploiting Zn2SnO4 Prepared in Solution below 100 °C. Nat. Commun. 2015, 6, 7410.

(30) Yao, K.; Wang, X.; Xu, Y.-x.; Li, F. A General Fabrication Procedure for Efficient and Stable Planar Perovskite Solar Cells: Morphological and Interfacial Control by In-Situ-Generated Layered Perovskite. Nano Energy 2015, 18, 165−175.

(31) Kaltenbrunner, M.; Adam, G.; Głowacki, E. D.; Drack, M.; Schwö diauer, R.; Leonat, L.; Apaydin, D. H.; Groiss, H.; Scharber, M. C.; White, M. S.; et al. Flexible High Power-per-Weight Perovskite Solar Cells with Chromium Oxide−Metal Contacts for Improved Stability in Air. Nat. Mater. 2015, 14, 1032.

(32) Schmidt, T. M.; Larsen-Olsen, T. T.; Carle, J. E.; Angmo, D.;´ Krebs, F. C. Upscaling of Perovskite Solar Cells: Fully Ambient Roll Processing of Flexible Perovskite Solar Cells with Printed Back Electrodes. Adv. Energy Mater. 2015, 5 (15), 1500569.

(33) Kim, B. J.; Kim, D. H.; Lee, Y.-Y.; Shin, H.-W.; Han, G. S.; Hong, J. S.; Mahmood, K.; Ahn, T. K.; Joo, Y.-C.; Hong, K. S.; et al. Highly Efficient and Bending Durable Perovskite Solar Cells: Toward a Wearable Power Source. Energy Environ. Sci. 2015, 8 (3), 916−921.

(34) Ha, J.; Kim, H.; Lee, H.; Lim, K.-G.; Lee, T.-W.; Yoo, S. Device Architecture for Efficient, Low-Hysteresis Flexible Perovskite Solar Cells: Replacing TiO2 With C60 Assisted by Polyethylenimine Ethoxylated Interfacial Layers. Sol. Energy Mater. Sol. Cells 2017, 161, 338−346.

(35) Yoon, H.; Kang, S. M.; Lee, J.-K.; Choi, M. Hysteresis-Free Low-Temperature-Processed Planar Perovskite Solar Cells with 19.1% Efficiency. Energy Environ. Sci. 2016, 9 (7), 2262−2266.

(36) Yoon, J.; Sung, H.; Lee, G.; Cho, W.; Ahn, N.; Jung, H. S.; Choi, M. Superflexible, High-Efficiency Perovskite Solar Cells Utilizing Graphene Electrodes: Towards Future Foldable Power Sources. Energy Environ. Sci. 2017, 10 (1), 337−345.

(37) Habisreutinger, S. N.; Leijtens, T.; Eperon, G. E.; Stranks, S. D.; Nicholas, R. J.; Snaith, H. J. Carbon Nanotube/Polymer Composites as a Highly Stable Hole Collection Layer in Perovskite Solar Cells. Nano Lett. 2014, 14 (10), 5561−5568.

(38) Subbiah, A. S.; Agarwal, S.; Mahuli, N.; Nair, P.; van Hest, M.; Sarkar, S. K. Stable p−i−n FAPbBr3 Devices with Improved Efficiency Using Sputtered ZnO as Electron Transport Layer. Adv. Mater. Interfaces 2017, 4, 1601143.

(39) Kogo, A.; Sanehira, Y.; Numata, Y.; Ikegami, M.; Miyasaka, T. Amorphous Metal Oxide Blocking Layers for Highly Efficient LowTemperature Brookite TiO2-Based Perovskite Solar Cells. ACS Appl. Mater. Interfaces 2018, 10 (3), 2224−2229.

(40) Zhou, J.; Meng, X.; Zhang, X.; Tao, X.; Zhang, Z.; Hu, J.; Wang, C.; Li, Y.; Yang, S. Low-Temperature Aqueous Solution Processed Zno as an Electron Transporting Layer for Efficient Perovskite Solar Cells. Mater. Chem. Front. 2017, 1, 802−806.

(41) Wang, K. C.; Shen, P. S.; Li, M. H.; Chen, S.; Lin, M. W.; Chen, P.; Guo, T. F. Low-Temperature Sputtered Nickel Oxide Compact Thin Film as Effective Electron Blocking Layer for Mesoscopic NiO/ CH3NH3PbI3 Perovskite Heterojunction Solar Cells. ACS Appl. Mater. Interfaces 2014, 6 (15), 11851−8.

(42) Ling, X.; Yuan, J.; Liu, D.; Wang, Y.; Zhang, Y.; Chen, S.; Wu, H.; Jin, F.; Wu, F.; Shi, G.; et al. Room-Temperature Processed Nb2O5 as the Electron-Transporting Layer for Efficient Planar Perovskite Solar Cells. ACS Appl. Mater. Interfaces 2017, 9 (27), 23181−23188.

(43) Kim, Y.-H.; Heo, J.-S.; Kim, T.-H.; Park, S.; Yoon, M.-H.; Kim, J.; Oh, M. S.; Yi, G.-R.; Noh, Y.-Y.; Park, S. K. Flexible Metal-Oxide Devices made by Room-Temperature Photochemical Activation of Sol−Gel Films. Nature 2012, 489, 128.

(44) Bretos, I.; Jimenez, R.; Ricote, J.; Calzada, M. L. LowTemperature Crystallization of Solution-Derived Metal Oxide Thin Films Assisted by Chemical Processes. Chem. Soc. Rev. 2018, 47 (2), 291−308.

(45) Huang, L.; Sun, X.; Li, C.; Xu, J.; Xu, R.; Du, Y.; Ni, J.; Cai, H.; Li, J.; Hu, Z.; et al. UV-Sintered Low-Temperature Solution-Processed SnO2 as Robust Electron Transport Layer for Efficient Planar Heterojunction Perovskite Solar Cells. ACS Appl. Mater. Interfaces 2017, 9 (26), 21909−21920.

(46) Zhu, M.; Liu, W.; Ke, W.; Clark, S.; Secor, E. B.; Song, T.-B.; Kanatzidis, M. G.; Li, X.; Hersam, M. C. Millisecond-Pulsed Photonically-Annealed Tin Oxide Electron Transport Layers for Efficient Perovskite Solar Cells. J. Mater. Chem. A 2017, 5 (46), 24110−24115.

(47) Anaraki, E. H.; Kermanpur, A.; Steier, L.; Domanski, K.; Matsui, T.; Tress, W.; Saliba, M.; Abate, A.; Gratzel, M.; Hagfeldt, A.; et al. Highly Efficient and Stable Planar Perovskite Solar Cells by SolutionProcessed Tin Oxide. Energy Environ. Sci. 2016, 9 (10), 3128−3134.

(48) Ren, X.; Yang, D.; Yang, Z.; Feng, J.; Zhu, X.; Niu, J.; Liu, Y.; Zhao, W.; Liu, S. F. Solution-Processed Nb:SnO2 Electron Transport Layer for Efficient Planar Perovskite Solar Cells. ACS Appl. Mater. Interfaces 2017, 9 (3), 2421−2429.

(49) Dong, Q.; Shi, Y.; Wang, K.; Li, Y.; Wang, S.; Zhang, H.; Xing, Y.; Du, Y.; Bai, X.; Ma, T. Insight into Perovskite Solar Cells Based on SnO2 Compact Electron-Selective Layer. J. Phys. Chem. C 2015, 119 (19), 10212−10217.

(50) Huang, L.; Li, R.; Chong, R.; Liu, G.; Han, J.; Li, C. Cl- Making Overall Water Splitting Possible on TiO2-based Photocatalysts. Catal. Sci. Technol. 2014, 4 (9), 2913−2918.

(51) Schwartz, A. J.; Cheung, Y.; Jevtic, J.; Pikelja, V.; Menon, A.; Ray, S. J.; Hieftje, G. M. New Inductively Coupled Plasma for Atomic Spectrometry: The Microwave-Sustained, Inductively Coupled, Atmospheric-Pressure Plasma (MICAP). J. Anal. At. Spectrom. 2016, 31 (2), 440−449.

(52) Anders, A.; Yushkov, G. Y. Low-Energy Linear Oxygen Plasma Source. Rev. Sci. Instrum. 2007, 78 (4), 043304.

(53) Pockett, A.; Eperon, G. E.; Peltola, T.; Snaith, H. J.; Walker, A.; Peter, L. M.; Cameron, P. J. Characterization of Planar Lead Halide Perovskite Solar Cells by Impedance Spectroscopy, Open-Circuit Photovoltage Decay, and Intensity-Modulated Photovoltage/Photocurrent Spectroscopy. J. Phys. Chem. C 2015, 119 (7), 3456−3465.

(54) Wang, Q. Fast Voltage Decay in Perovskite Solar Cells Caused by Depolarization of Perovskite Layer. J. Phys. Chem. C 2018, 122 (9), 4822−4827.

(55) Pockett, A.; Eperon, G. E.; Sakai, N.; Snaith, H. J.; Peter, L. M.; Cameron, P. J. Microseconds, Milliseconds and Seconds: Deconvoluting the Dynamic Behaviour of Planar Perovskite Solar Cells. Phys. Chem. Chem. Phys. 2017, 19 (8), 5959−5970.

(56) Jiang, Y.; Juarez-Perez, E. J.; Ge, Q.; Wang, S.; Leyden, M. R.; Ono, L. K.; Raga, S. R.; Hu, J.; Qi, Y. Post-Annealing of MAPbI3 Perovskite Films with Methylamine for Efficient Perovskite Solar Cells. Mater. Mater. Horiz. 2016, 3 (6), 548−555.

(57) Mohammadian, N.; Moshaii, A.; Alizadeh, A.; Gharibzadeh, S.; Mohammadpour, R. Influence of Perovskite Morphology on Slow and Fast Charge Transport and Hysteresis in the Perovskite Solar Cells. J. Phys. Chem. Lett. 2016, 7 (22), 4614−4621.